The growth process of saponite: A study based on particle size distributions and morphological evolution

Chaoqun Zhang, Hongping He, Xiaorong Qin, Alain Decarreau, Fabien Baron, Qi Tao, Jianxi Zhu, Yunfei Xi, Sabine Petit

The growth process of saponite: A study based on particle size distributions and morphological evolution

Chaoqun Zhang[a], Hongping He[a, c, d], Xiaorong Qin[a, d], Alain Decarreau[b], Fabien Baron[b], Qi Tao[a], Jianxi Zhu[a, c, d], Yunfei Xi[e], Sabine Petit[b*]

[a] CAS Key Laboratory of Mineralogy and Metallogeny/Guangdong Provincial Key Laboratory of Mineral Physics and Materials, Guangzhou Institute of Geochemistry, Chinese Academy of Sciences, Guangzhou 510640, China

[b] Institut de Chimie des Milieux et Matériaux de Poitiers (IC2MP), UMR 7285 CNRS, Université de Poitiers, F-86073 Poitiers Cedex 9, France

[c] CAS Center for Excellence in Deep Earth Science, Guangzhou, 510640, China

[d] University of Chinese Academy of Sciences, Beijing 100049, China

[e] Central Analytical Research Facility (CARF) / School of Chemistry and Physics-Faculty of Science, Queensland University of Technology (QUT), Brisbane, Queensland 4001, Australia

*Corresponding Author

E-mail: sabine.petit@univ-poitiers.fr (Prof. Sabine PETIT)

Post address: UMR 7285 CNRS, Université de Poitiers, F-86073 Poitiers Cedex 9, France

Abstract

Smectite growth is of great importance for the geochemistry of clay minerals on the Earth's surface and their applications in industries. However, the growth process and mechanism controlling the physicochemical properties of smectite are still poorly understood. Through an effective integration of particle size distributions (PSDs) and morphology of particles, this study has enhanced the understanding of smectite growth by investigating the growth processes of a synthetic tri-octahedral smectite (saponite). The starting materials were equimolar Mg-saponite and Ni-saponite that had been hydrothermally synthesised at 220°C. Two Mg–Ni-saponite samples were obtained through further hydrothermal treatment of the starting materials at 400 and 500°C. A systematic measurement of the size in the *ab*-plane of numerous saponite particles was performed to obtain their PSDs. The parameters α and β^2, derived from PSDs and the morphology of saponite, indicate that saponites grow mainly via surface-controlled growth and likely via supply-controlled growth in open systems. Particle attachment via the edge surfaces of saponite is an accompanying growth mechanism, and talc-like layers favour the "three-dimensional growth". In addition, the heterogeneous tetrahedral Al distribution of saponite could lead to the formation of elongated laths.

Keywords: Crystal growth; particle size distribution (PSD); saponite; particle attachment; smectite morphology

1. Introduction

The smectite group of clay minerals, composed of a central octahedral sheet and two tetrahedral sheets, has attracted particular attention due to their geochemical significance (Eberl, 1984; Tardy et al., 1987; Sposito et al., 1999; Merriman et al., 2005; Christidis and Huff, 2009; Voigt et al., 2020) and wide applications (Odom, 1984; Murray, 1991; Bergaya and Lagaly, 2013). Its formation processes, including phase transformation and crystal growth, not only affect its applications in industries but also respond to the physicochemical environment where it formed. The alteration of other minerals into smectite has been extensively studied (e.g., Badaut, et al., 1983; Banfield et al., 1994; Cuadros et al., 2012; Tao et al., 2019). However, only a few studies on smectite growth have been made available thus far, owing to the limitations of its special properties (e.g., complex compositions, hydrated layers, and small particle size) (Christidis 2001; Decarreau et al., 2014; Zhang et al., 2020; Besselink et al., 2020).

The particle size distribution (PSD) of a mineral has a distinctive shape related to its growth history. It is possible to describe the mineral growth processes based on their measured PSDs (Wagner, 1961; Baronnet, 1982). Eberl et al. (1998) simulated PSDs of different crystal growth patterns in closed and open systems. An open system is defined as a system in which matter is supplied to the growing crystals by a source other than the growing phase; whereas a closed system is defined as a system where a single phase is involved, and the less stable crystals dissolve to supply materials for the growth of other crystals. Eberl et al. (1998) defined surface-controlled growth in open systems when crystals grow with an essentially unlimited supply of nutrients, and the dissolution rate of the "source" is not the limiting factor. Supply-controlled growth in open systems refers to the rate of crystal growth, which is controlled by the

77 rate of nutrients. Ostwald ripening in closed systems is a recrystallisation process in a
78 closed system that is characterized by the simultaneous dissolution and growth of a
79 mineral in a single medium (Wagner et al., 1961). In such a system, large particles
80 grow at the expense of dissolving small particles, resulting in the minimization of
81 surface free energy (Lifshitz and Slyozov, 1961).

82 Środoń et al. (2000) measured PSDs of natural illite and illite-smectite using
83 transmission electron microscopy (TEM) and concluded that illite grew through
84 surface-controlled growth in open systems. Christidis (2001) also applied the PSD
85 model of Eberl et al. (1998) to the investigation of the growth mechanisms of smectite
86 in a natural system. Their results indicated that smectite experiences supply-controlled
87 growth in an open system and random ripening in a closed system. Zhang et al. (2020)
88 studied the growth process of synthetic saponite by combining PSDs of particle
89 measurements obtained from scanning transmission electron microscopy (STEM)
90 images, argon adsorption, and crystal chemistry. Obtained results implied that
91 saponite growth proceeds via a lateral extension of layers by surface-controlled
92 growth in an open system.

93 Natural smectite has complex compositions, and in particular its early stages
94 of growth cannot be reprised. Thus, a synthetic laboratory approach has been
95 extensively used to investigate the crystal growth of smectite (e.g., Kloprogge et al.,
96 1999; Zhang et al., 2010; Petit et al., 2017). It should be noted that a smectite 'crystal'
97 is more comparable to an assemblage of layers than a true crystal (Lagaly and Dékany,
98 2013), and smectite growth essentially consists of a two-dimensional lateral extension
99 of layers (Decarreau et al., 2014; Zhang et al., 2020). Thus, the PSDs obtained by
100 recording the crystal size in the *ab*-plane of particles are useful for studying smectite
101 growth.

In this study, the growth processes of endmember Mg-saponite and Ni-saponite synthesised at 220°C, and two Mg–Ni-saponites synthesised at 400 and 500°C, respectively, were investigated through a combination of PSDs and morphologies. The diameters of numerous synthetic saponite particles were measured from STEM images to obtain a series of PSD models. These PSD models were further used to discuss the growth history of saponite.

2. Materials and Methods

2.1. Synthesis of samples

The synthesis and characterisation of the saponites used in this study have been described in detail by Zhang et al. (2021). Briefly, Mg-saponite and Ni-saponite precursors were synthesised by the hydrothermal treatment (220°C, 1 d) of a co-precipitated gel with a theoretical molar ratio of Si:Al:Mg = 3.7:0.3:3. The Mg-saponite and Ni-saponite precursors were named pMg220 and pNi220, respectively. The starting material for Mg–Ni-saponite synthesis was prepared by mixing identical molar weights of pMg220 and pNi220, and named pMg220+pNi220. Two samples were obtained by hydrothermal treatment of the starting material at 400 and 500°C, and were named 220-400 and 220-500, respectively.

2.2. Characterizations of synthetic saponites

Powder X-ray diffraction (XRD) patterns were obtained using a Bruker D8 advance diffractometer (CuKα radiation, 40 kV and 40 mA) over the range of 2–65° (2θ) with a 0.025° (2θ) step size and 0.6 s per step, while the patterns of the oriented samples and ethylene glycol treated samples were collected over the range of 2–15° (2θ). The randomly oriented samples were prepared by pressing the saponite powder inside a cavity up to the reference level of the sample holders. The oriented samples

were prepared by carefully pipetting the clay suspension onto a glass slide and allowing it to dry at ambient temperature. Ethylene glycol treated samples were prepared by treating the oriented samples in a glass desiccator with ethylene glycol at 25°C for 24 h.

High-angle annular dark-field scanning transmission electron microscopy (HAADF-STEM) observations were performed to investigate the morphology of the saponite particles in the *ab*-plane. A mixture of 1 mg of sample and 10 ml of deionised water was lightly stirred for one week to obtain a diluted colloidal suspension. The specimens were prepared by dispersing the colloidal suspension in 40 ml of ethanol and treating them ultrasonically for 30 min. A drop of the resultant suspension was placed on a porous carbon film supported by a copper grid, then water and ethanol were evaporated. STEM images were obtained using an FEI Talos F200S high-resolution transmission electron microscope operated at 200 kV.

2.3. Measurement of PSDs

The saponite growth studied in this study was based on the two-dimensional extension of the particles in the *ab*-plane. Zhang et al. (2020, 2021) successfully observed well-dispersed particles of synthetic saponite by STEM and measured the size of a series of particles to obtain their PSDs by taking the mean value of length plus width in the *ab*-plane. Because saponite particles are generally irregularly shaped, we have developed a new method to measure the particle size of saponite, which is more accurate than that in Zhang et al. (2020) (Fig. 1). After obtaining well-dispersed saponite particles from STEM images, the area of the *ab*-plane of a particle was calculated using Image-ProPlus 6.0 software package in a manual mode. Then, the obtained area was treated as a circle with a calculable diameter (d) that represents the mean size of the particle. The number of measured saponite particles to obtain PSDs

was close to 1500 (1508 for 220-400, 1434 for 220-500, 1325 for pMg220, and 1499 for pNi220). The experimental PSD curves were simulated using a log-normal distribution function. Parameter α describes the mean of natural logarithms of observations *d* (diameter), with $\alpha = \sum(\ln d)\mathrm{f}(d)$; while β^2 describes the variance of natural logarithms of observations *d*, with $\beta^2 = \sum[\ln(d) - \alpha]^2 \mathrm{f}(d)$; where f(*d*) is the frequency of *d* (Eberl et al., 1998).

3. Results and discussion

3.1. Crystal habit

Powder XRD patterns of Mg-saponite (pMg220) and Ni-saponite (pNi220) precursors displayed characteristic reflections of tri-octahedral smectite with the (001) reflection at ~1.25 nm, the (06, 33) at 0.153 nm, and asymmetric *(hk)* reflections (Fig. 2), as described by Zhang et al. (2021). Compared with that of pMg220, the broader reflections for pNi220 suggested that the coherent scattering domains in the layer plane, as well as the number of stacked layers, are smaller for Ni-saponite than for Mg-saponite. The XRD patterns of the oriented samples display the characteristic reflections of saponites with a basal spacing d(001) at ~1.2 nm, which shifts to 1.72 nm after exposure to ethylene glycol (Fig. 3) (Zhang et al., 2021). For 220-500, reflections at 2.58 nm and 3.07 nm are observed before and after ethylene glycol treatment (Fig. 3), respectively. The difference between these two values is ~0.5 nm, comparable to the difference between 1.20 nm and 1.72 nm, presumably due to the occurrence of interstratified non-swelling layers (Whitney, 1983). The non-swelling layers are likely low-charge talc-like layers according to the low pre-set layer charge of saponite (0.3) (Christidis and Mitsis, 2006; Petit et al., 2008; Fonteneau et al., 2020).

The STEM images provided detailed morphological information on the *ab*-plane of the particles of all saponites (Figs. 4-5). The layers of pMg220 were generally irregular in shape (Fig. 4a), whereas those of pNi220 exhibited geometrically hexagonal shapes (Fig. 4b). It was noted that some elongated laths and 120° angles between lateral faces occur in sample pMg220, which were also observed in Kozákov natural saponite (Suquet et al., 1975). The elongated laths were also observed in nontronite and hectorite, and were identified as elongations along the *a*-axis (Mering and Oberling, 1967). Figure 5 reveals an increase in particle size from the starting materials to obtained samples (220-400 and 220-500), providing evidence of saponite particle growth. At higher temperatures, more euhedral elongated particles were observed.

3.2. PSDs of Mg-saponite, Ni-saponite, and Mg-Ni saponite

The shape of the PSDs and the reduced PSD profiles of Mg-saponite, Ni-saponite, and Mg-Ni saponite were approximately log-normal (Figs. 6-8). The diameters of the pMg220 particles were in the range of 10–450 nm, with most of them fell within the range of 10–200 nm (Fig. 6a). In contrast, the diameter of the pNi220 particles varied from 5 to 250 nm, and most of them were in the range of 5–120 nm (Fig. 6c). The mean particle diameter in pNi220 was 36.7 nm, which was far less than that of pMg220 (87.2 nm) (Table 1).

The PSD of sample 220-400 had a log-normal shape with a range of 10–500 nm (Fig. 7a). Meanwhile, from the starting materials to 220-400, the mean diameter of the particles increases from 58.2 to 79.2 nm (Table 1), which indicates the growth of saponite layers. The PSD of sample 220-500 overall displayed a log-normal shape with several secondary maxima in the range of 30–850 nm (Fig. 8a). From the starting material to 220-500, the mean diameter increased from 58.2 to 156.8 nm (Table 1),

suggesting a strong growth of saponite particles. Zhang et al. (2021) provided a comprehensive FTIR analysis on the evolutionary processes of the starting material (pMg220+pNi220) into the samples (220-400 and 220-500). The results indicated that partial dissolution (~0.59) of the starting material and recrystallisation of Mg–Ni-saponite occurred in sample 220-400, whereas a total dissolution of the starting material and recrystallisation of Mg–Ni-saponite occurred in sample 220-500. Thus, saponite growth for both samples proceeded via dissolution of the starting material and the recrystallisation of Mg–Ni-saponite.

3.3. Ripening process

Eberl et al. (1998) summarised the crystal growth (ripening) mechanisms based on the dissolution–recrystallisation mechanism. The log-normal shape of PSDs (Figs. 6–8) and the coordinates of (α, β^2) (Fig. 9) can be used to discuss the ripening processes of the saponite (Eberl et al., 1998; Środoń et al., 2000). Generally, a log-normal shape may imply that crystal growth follows either Ostwald ripening or random ripening in a closed system, and surface-controlled growth or supply-controlled growth in an open system, according to the α and β^2 values (Fig. 9). Following the definitions of open or closed systems (see Introduction), the systems discussed in this study are open systems, because the source and the growing crystals are not in the same phase. The source of pMg220 and pNi220 were co-precipitated gels, comprising Mg-saponite and Ni-saponite compositions, respectively; whereas the source of Mg–Ni-saponites (220-400 and 220-500) was the starting material (pMg220+pNi220). Furthermore, the log-normal shape of PSD and reduced PSD profiles for pMg220, pNi220, and 220-400 are heavily skewed to the left (Figs. 6–7), which indicates supply-controlled growth or surface-controlled growth in open systems (Eberl et al., 1998).

The coordinates of (α, β^2) provided more information about the ripening processes. For pMg220 and sample 220-400, the coordinates of (α, β^2) (Table 1) in open systems placed them close to the line of surface-controlled growth (Fig. 9). These results are also consistent with the surface–controlled growth of Mg–Ni-saponite reported by Zhang et al. (2020). For pMg220, the source refers to the co-precipitated gel and the growing crystals of Mg-saponite, whereas for 220-400, the starting material (pMg220+pNi220) is the source and Mg–Ni-saponite form the growing crystals. Surface-controlled growth proceeds through incorporating the species from the dissolution/disarticulation of the source into the growth surface, and the concentration of the species on the growth surface is the same as that in the source (Konak et al., 1974; Eberl et al., 1998). Thus, for pMg220 and 220-400, the dissolution/ disarticulation rate of the source is not the limiting factor (Eberl et al., 1998). In such systems, the surface free energy then tends toward a minimum by the dis-articulation/dissolution of the source and growth of the neoformed saponite. As a result, the mean diameter increases (e.g., from 58.2 nm to 79.2 nm in sample 220-400) (Table 1; Fig. 5), and finally, the level of supersaturation in the solution decreases (Lifshitz and Slyozov, 1961; Wagner, 1961).

For pNi220, the point of (α, β^2) locates on the line of supply-controlled growth in open systems, near the intersection with the line of surface-controlled growth in open systems (Fig. 9). Decarreau (1985) demonstrated that Ni-smectites are generally less soluble than Mg-smectites in a hydrothermal environment. pMg220 and pNi220 were synthesised from co-precipitated gels containing "embryos" (germs) of saponite (Zhang et al., 2021). Consequently, Mg-containing gels dissolved more easily than Ni-containing gels. The mean diameter of the pNi220 particles was half that of pMg220 (Table 1), indicating a less efficient crystal growth process for Ni-saponite.

The low kinetics of pNi220 crystal growth are likely linked to the low solubility of Ni-containing gel, which limits the transformation of the gel into Ni-saponite in the aqueous system and induces a partially supply-controlled growth process.

3.4. Non-classical crystal growth of saponite

The PSD and reduced PSD profile of sample 220-500 displayed a mean log-normal shape with several small secondary maxima (Fig. 8). However, the coordinate of (α, β^2) for sample 220-500 is placed neither on the surface-controlled line nor the supply-controlled line, suggesting that this sample may undergo complex ripening processes (Fig. 9). Eberl et al. (1998) proposed that agglomeration growth may occur simultaneously with ripening, leading to multimodal distributions. The STEM observations provided direct evidence for attachments between saponite particles (Fig. 10). As shown in Figure 10a, a smaller particle (marked by 1) attaches to a larger particle (marked by 2) by their edge surfaces (marked by red arrows), where the gap (red dotted line) suggests that the fusion between both particles is likely ongoing. The irregularly shaped particle in Figure 10b is composed of at least three sub-particles, that is, the elongated lath (labelled "3") and two irregular particles (labelled "1" and "2"). In sample 220-500, several secondary maxima resulted from non-classical crystal growth (i.e., particle attachment) (Wang et al., 2014). Thus, both indeterminate ripening and particle attachment were involved in the formation of Mg–Ni-saponite in sample 220-500. Particle attachment was also sporadically observed in the STEM images of sample 220-400 (Fig. S1), where saponite growth proceeded via the fusion of the particle edges (red dotted line). Thus, in sample 220-400, particle attachment occurred simultaneously with surface-controlled ripening but was too imperceptible to be recorded by the PSD model (Fig. 7). For two adjacent particles (Figs. 10 and S1), there is the possibility that one particle is preferentially growing at the expense of the

other one, because heterogeneity in composition from one particle to another may drive such preferential dissolution and growth. Such viewpoint could be confirmed by *in situ* observation during saponite growth processes when the technology is feasible.

It was reported that crystal growth by particle attachment occurs widely in geochemical, biological, and synthetic material systems (De Yoreo et al., 2015). However, there is little research on the non-traditional growth of clay minerals. García-romero et al. (2018) used a TEM to locate and identify smectite and kaolinite particles that seemed to originate from non-classical crystal growth. Furthermore, the authors proposed for the first time that growth by particle attachment is present in clay minerals, and such growth patterns are related to the depositional environments. Zhang et al. (2020) found that the size of Mg–Ni-saponite layers significantly increased with a slight increase in the degree of dissolution in its corresponding precursors, and proposed the existence of non-classical growth during the formation of Mg–Ni-saponite in a hydrothermal synthesis system. He et al. (2021) performed TEM on natural biotite, natural muscovite, and synthetic fluorophlogopite. Their results showed that in addition to the traditional crystal growth mechanism, the oriented attachment of particles is common in the growth process of mica. A non-classical crystallisation model was proposed for the formation of phyllosilicates at elevated temperatures in magmatic and metamorphic environments, where the oriented attachment of building blocks occurs; frequently along the (001) plane or the [001] direction, or both simultaneously (He et al., 2021). Such a study not only showed that non-classical crystal growth patterns are widespread in phyllosilicates, but also extended the observations of particle attachment to magma and high-grade metamorphic processes. In this study, the combination of PSDs and morphology provided evidence that the non-classical growth of clay minerals may exist in high-

temperature hydrothermal environments. These results provide important references for further research on the genesis of complex clay minerals and related geochemical processes.

3.5. Crystal growth process

Meunier (2006) had applied the periodic bond chain (PBC) theory of Hartman (1973) to the crystal growth in clay minerals, which essentially implied a two-dimensional extension of clay minerals within the (001) plane. For smectite, it is not clear whether the extensional crystals are composed of stacked multi-layers or a single layer (Meunier, 2006; Decarreau et al., 2014).

In this study, in the saponite synthesised at 220°C, it appears that the well-dispersed particles are single layers (Fig. 4). For saponite, the hydrated interlayer cations could hinder a stack and thus the dominant growth pattern is the two-dimensional lateral growth of single layer (or a few layers). These saponite layers stack layer by layer randomly during the process of water loss, leading to heterogeneous saponite particles. In the sample synthesised at 500°C, some observed particles clearly consisted of several stacked layers (Fig. 10), suggesting a different crystal growth process. The XRD patterns of 220-500 indicated the occurrence of talc-like layers (Fig. 3), which have low (no) interlayer charge and easily stack into relatively homogeneous crystals with similar dissolution/growth behaviour. Consequently, 220-500 can grow following, at least partly, a three-dimensional structure, similar to other clay minerals.

The PBCs present in this study were those within the (001) plane, that is, the PBCs of [100], [110], and [$\bar{1}$10]. The growth faces of the crystal were observed lying parallel to one or more continuous PBCs. Al distribution can affect the shape of

saponite by controlling the development of PBCs (Meunier, 2006). In this study, saponite with a very low charge (0.3) most likely led to the heterogeneous distribution of tetrahedral Al, which induced defects in the saponite layers. Such defects may hinder the development of PBCs in saponite structures. The occurrence of elongated laths in saponites (pMg220, 220-400, and 220-500) likely suggests that only one PBC is favoured in the saponite structure. For Ni-saponite (pNi220), the small layers with a relatively regular shapes like hexagons may indicate that all PBCs are affected.

4. Conclusions

The present study combines the PSD model and STEM observations to investigate the growth processes of synthetic saponite. The results have indicated that saponite particle growth proceeds mainly via surface-controlled growth and possibly via supply-controlled growth in closed systems, based on the shape of the PSDs and the plotted coordinates of (α, β^2) following Eberl et al. (1998)'s model. Particle attachment, which leads to a multimodal PSD shape, is probably a corresponding growth mechanism. The heterogeneous Al distribution of the low-charge saponite could lead to the formation of elongated laths, and talc-like layers which favour the "three-dimensional growth" of saponite in high-temperature environments.

5. Acknowledgment

We appreciate the financial supports by National Natural Science Foundation of China (Grant Nos. 41921003, 41825003, 42072044), Science and Technology Planning of Guangdong Province, China (2020B1212060055), The European Union (ERDF), "Région Nouvelle Aquitaine," French « Ministère de l'Enseignement Supérieur et de la Recherche », The Clay Minerals Society, and China Scholarship Council.

References

Badaut, D., Risacher, F., 1983. Authigenic smectite on diatom frustules in Bolivian saline lakes. Geochim Cosmochim Ac 47, 363-375.

Banfield, J., Barker, W., 1994. Direct observation of reactant-product interfaces formed in natural weathering of exsolved, defective amphibole to smectite: Evidence for episodic, isovolumetric reactions involving structural inheritance. Geochim Cosmochim Ac 58, 1419-1429.

Baronnet, A., 1982. Ostwald ripenning in solution: the case of calcite and mica. Estudios geológicos 38, 185-198.

Besselink, R., Stawski, T.M., Freeman, H.M., Hövelmann, J., Tobler, D.J., Benning, L.G., 2020. Mechanism of Saponite Crystallization from a Rapidly Formed Amorphous Intermediate. Crystal Growth & Design 20, 3365-3373.

Carrado, K., Decarreau, A., Petit, S., Bergaya, F., Lagaly, G., 2006. Synthetic clay minerals and purification of natural clays. Developments in clay science 1, 115-139.

Christidis, G.E., 2001. Formation and growth of smectites in bentonites: a case study from Kimolos Island, Aegean, Greece. Clays and Clay Minerals 49, 204-215.

Christidis, G.E., Huff, W.D., 2009. Geological aspects and genesis of bentonites. Elements 5, 93-98.

Christidis, G.E., and Mitsis, I., 2006. A new Ni-rich stevensite from the ophiolite complex of Othrys, Central Greece. Clays and Clay Minerals 54, 653-666.

Cuadros, J., 2012. Clay crystal-chemical adaptability and transformation mechanisms. Clay Minerals 47, 147-164.

De Yoreo, J.J., Gilbert, P.U.P.A., Sommerdijk, N.A.J.M., Penn, R.L., Whitelam, S., Joester, D., Zhang, H.Z., Rimer, J.D., Navrotsky, A., Banfield, J.F., Wallace, A.F., Michel, F.M., Meldrum, F.C., Colfen, H., Dove, P.M., 2015. Crystallization by particle attachment in synthetic, biogenic, and geologic environments. Science 349.

Decarreau, A., 1985. Partitioning of divalent transition elements between octahedral sheets of trioctahedral smectites and water. Geochim Cosmochim Ac 49, 1537-1544.

Decarreau, A., Petit, S., Andrieux, P., Villieras, F., Pelletier, M., Razafitianamaharavo, A., 2014. Study of Low-Pressure Argon Adsorption on Synthetic Nontronite: Implications for Smectite Crystal Growth. Clays and Clay Minerals 62, 102-111.

Eberl, D., 1984. Clay mineral formation and transformation in rocks and soils. Philosophical Transactions of the Royal Society of London. Series A, Mathematical and Physical Sciences 311, 241-257.

Eberl, D., Drits, V., Srodon, J., 1998. Deducing growth mechanisms for minerals from the shapes of crystal size distributions. American journal of Science 298, 499-533.

Fonteneau, L., Caner, L., Petit, S., Juillot, F., Ploquin, F., Fritsch, E., 2020. Swelling capacity of mixed talc-like/stevensite layers in white/green clay infillings ("deweylite"/"garnierite") from serpentine veins of faulted peridotites, New Caledonia. American Mineralogist 105, 1536-1546.

García-Romero, E., Suárez, M., 2018. A structure-based argument for nonclassical crystal growth in natural clay minerals. Mineralogical Magazine 82, 171-180.

He, H., Yang, Y., Ma, L., Su, X., Xian, H., Zhu, J., Teng, H.H., Guggenheim, S., 2021. Evidence for a two-stage particle attachment mechanism for phyllosilicate crystallization in geological processes. American Mineralogist 106, 983-993.

Hartman P., 1973. Structure and morphology. In Crystal Growth: an Introduction (P. Hartman editor), pp 367-402. North-Holland Publications, Amsterdam.

Kloprogge, J.T., Komarneni, S., Amonette, J.E., 1999. Synthesis of smectite clay minerals: a critical review. Clays and Clay Minerals 47, 529-554.

Konak, A., 1974. A new model for surface reaction-controlled growth of crystals from solution. Chemical Engineering Science 29, 1537-1543.

Lagaly, G., Dékány, I., 2013. Chapter 8 - Colloid Clay Science, in: Bergaya, F., Lagaly, G. (Eds.), Developments in Clay Science. Elsevier, pp. 243-345.

401 Lifshitz, I.M., Slyozov, V.V., 1961. The kinetics of precipitation from supersaturated solid
402 solutions. Journal of Physics and Chemistry of Solids 19, 35-50.
403 Mering, J., Oberlin, A., 1967. Electron-Optical Study of Smectites. Clays and Clay Minerals
404 15, 3-25.
405 Merriman, R.J., 2005. Clay minerals and sedimentary basin history. Eur J Mineral 17, 7-20.
406 Meunier, A., 2006. Why are clay minerals small? Clay Minerals 41, 551-566.
407 Murray, H.H., 1991. Overview — clay mineral applications. Applied Clay Science 5, 379-395.
408 Odom, I. E., 1984. Smectite clay minerals: properties and uses. Philosophical Transactions of
409 the Royal Society of London. Series A, Mathematical and Physical Sciences 311, 391
410 -409.
411 Penn, R.L., Banfield, J.F., 1998. Oriented attachment and growth, twinning, polytypism, and
412 formation of metastable phases: Insights from nanocrystalline TiO_2. American
413 Mineralogist 83, 1077-1082.
414 Petit, S., Baron, F., Decarreau, A., 2017. Synthesis of nontronite and other Fe-rich smectites:
415 a critical review. Clay Minerals 52, 469-483.
416 Petit, S., Righi, D., Decarreau, A., 2008. Transformation of synthetic Zn-stevensite to Zn-talc
417 induced by the hofmann-klemen effect. Clays and Clay Minerals 56, 645-654.
418 Sposito, G., Skipper, N.T., Sutton, R., Park, S.-h., Soper, A.K., Greathouse, J.A., 1999.
419 Surface geochemistry of the clay minerals. Proceedings of the National Academy of
420 Sciences 96, 3358-3364.
421 Środoń, J., Eberl, D.D., Drits, V.A., 2000. Evolution of Fundamental-Particle Size during
422 Illitization of Smectite and Implications for Reaction Mechanism. Clays and Clay
423 Minerals 48, 446-458.
424 Suquet, H., Malard, C., Copin, E., Pezerat, H., 1981. Variation du paramètre b et de la
425 distance basale d 001 dans une série de saponites à charge croissante: I. Etats hydratés.
426 Clay Minerals 16, 53-67.

Tardy, Y., Duplay, J., Fritz, B., 1987. Stability fields of smectites and illites as a function of temperature and chemical composition. Swedish Nuclear Fuel and Waste Management Co.

Tao, Q., Zeng, Q., Chen, M., He, H., Komarneni, S., 2019. Formation of saponite by hydrothermal alteration of metal oxides: Implication for the rarity of hydrotalcite. American Mineralogist 104, 1156-1164.

Voigt, M., Pearce, C.R., Fries, D.M., Baldermann, A., Oelkers, E.H., 2020. Magnesium isotope fractionation during hydrothermal seawater-basalt interaction. Geochim Cosmochim Ac 272, 21-35.

Wagner, C., 1961. Theorie der Alterung von Niederschlägen durch Umlösen (Ostwald-Reifung). 65, 581-591.

Whitney, G., 1983. Hydrothermal reactivity of saponite. Clays and Clay Minerals 31, 1-8.

Zhang, C., He, H., Petit, S., Baron, F., Tao, Q., Gregoire, B., Zhu, J., Yang, Y., Ji, S., Li, S., 2021. The evolution of saponite: An experimental study based on crystal chemistry and crystal growth. American Mineralogist 106, 909-921.

Zhang, C., Petit, S., He, H., Villiéras, F., Razafitianamaharavo, A., Baron, F., Tao, Q., Zhu, J., 2020. Crystal Growth of Smectite: A Study Based on the Change in Crystal Chemistry and Morphology of Saponites with Synthesis Time. ACS Earth and Space Chemistry 4, 14-23.

Zhang, D., Zhou, C., Lin, C., Tong, D., Yu, W., 2010. Synthesis of clay minerals. Applied Clay Science 50, 1-11

Figures and Tables

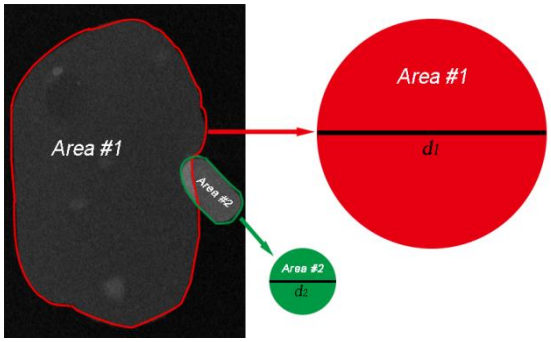

Fig. 1. Schematic measurement process of saponite particle size (diameter) in the *ab*-plane.

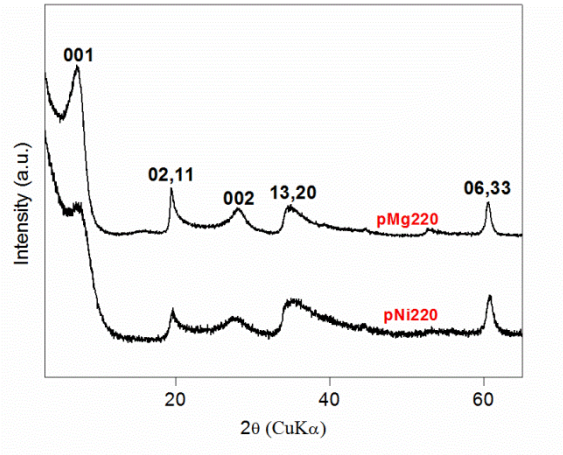

Fig. 2. Powder XRD patterns of synthetic Mg-saponite (pMg220) and Ni-saponite (pNi220) precursors.

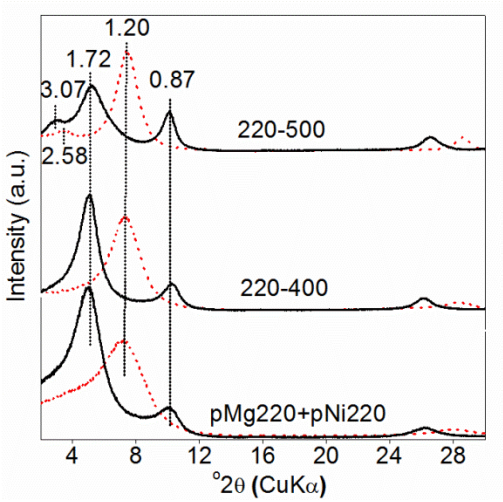

Fig. 3. XRD patterns of oriented samples (air-dried — red dot; after glycolation — black solid).

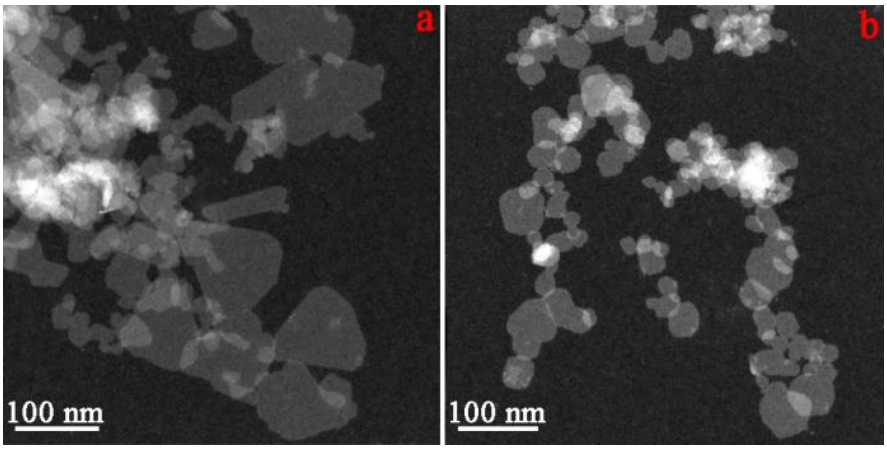

Fig. 4. STEM images of synthetic precursors: (a) Mg-saponite (pMg220), and (b) Ni-saponite (pNi220).

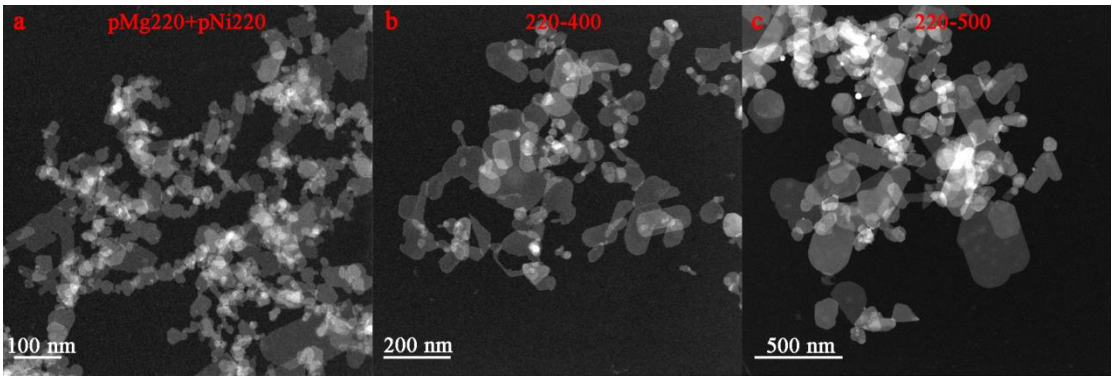

Fig. 5. STEM images of the starting materials (a) (pMg220+pNi220), (b) sample 220-400, and (c) sample 220-500.

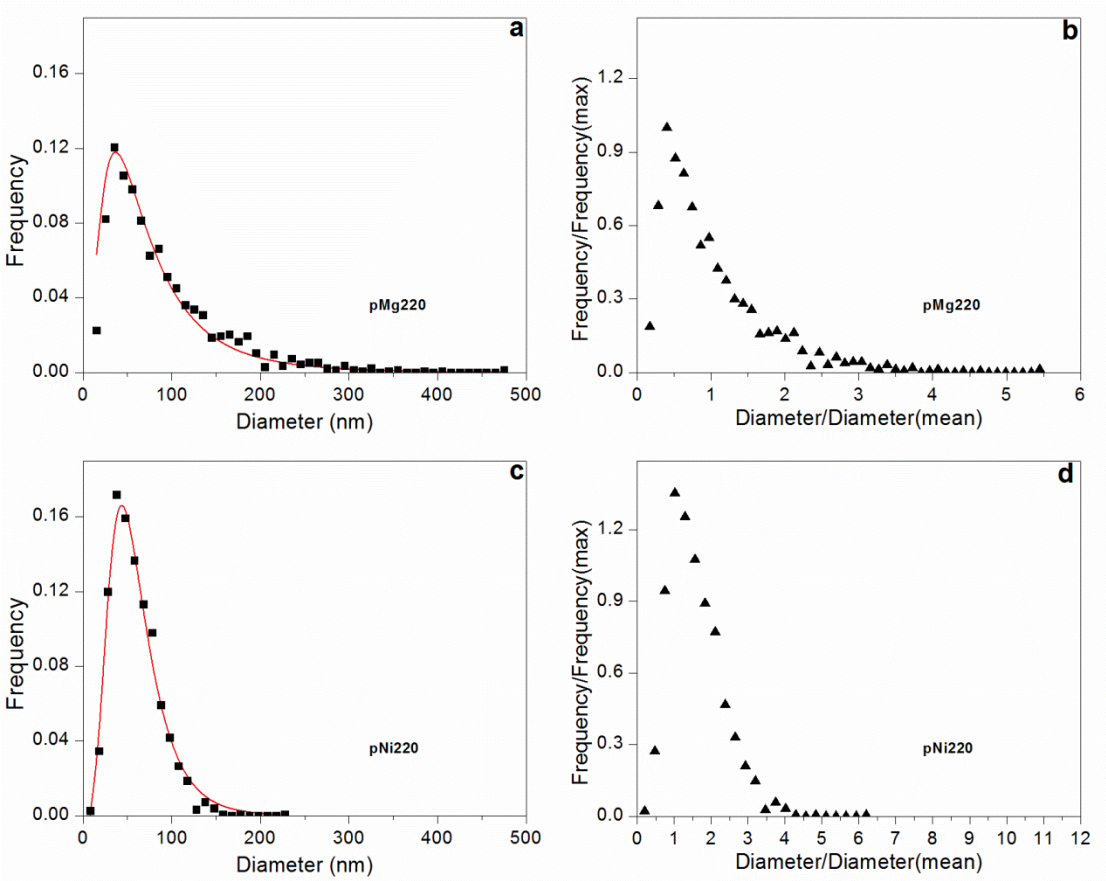

Fig. 6. Particle size distributions (PSDs) and PSD reduced profiles of synthetic saponites: (a–b) Mg-saponite (pMg220), and (c–d) Ni-saponite (pNi220).

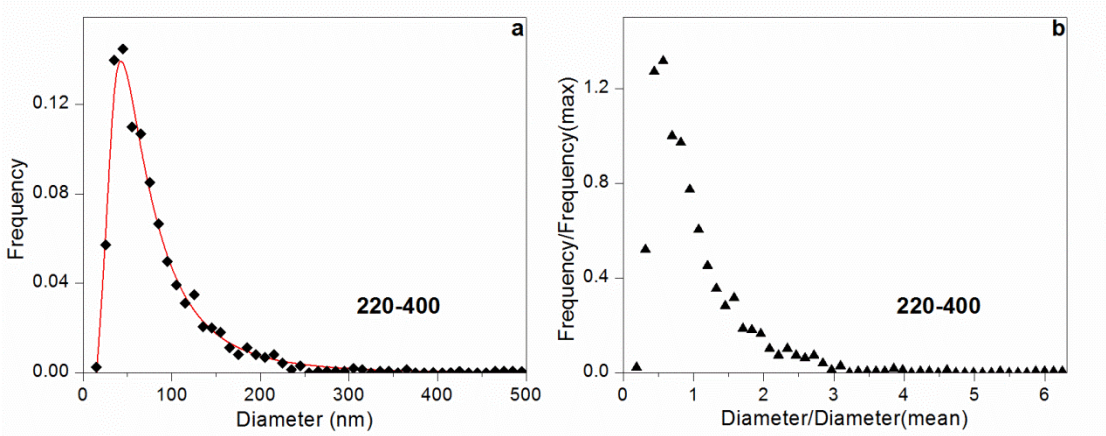

Fig. 7. PSD (a) and PSD reduced profile (b) of sample 220-400.

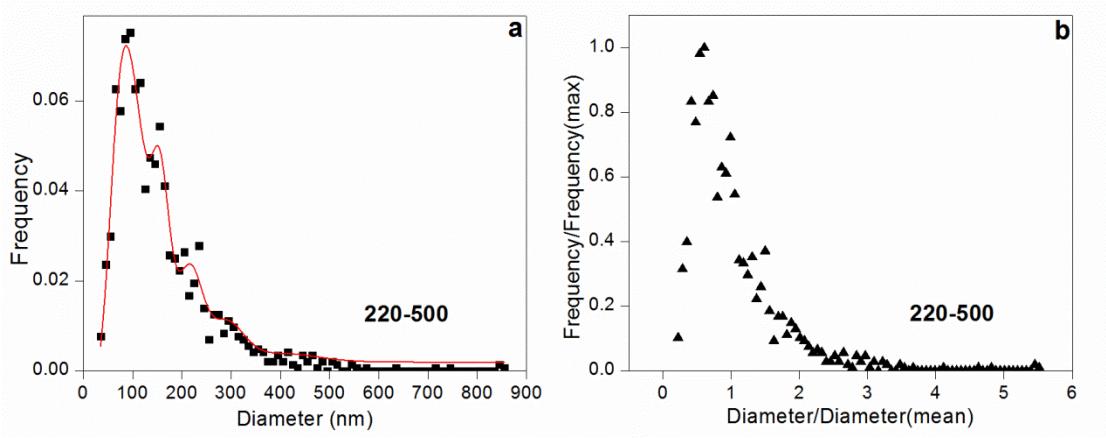

Fig. 8. PSD (a) and PSD reduced profile (b) of sample 220-500.

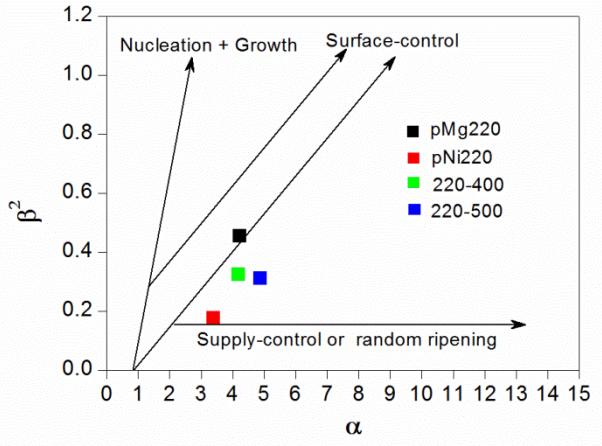

Fig. 9. Simple diagram of variations in $\alpha-\beta^2$ of synthetic Mg-saponite (pMg220), Ni-saponite (pNi220), and Mg–Ni-saponite (220-400, and 220-500), plotted on the diagram of Eberl et al. (1998).

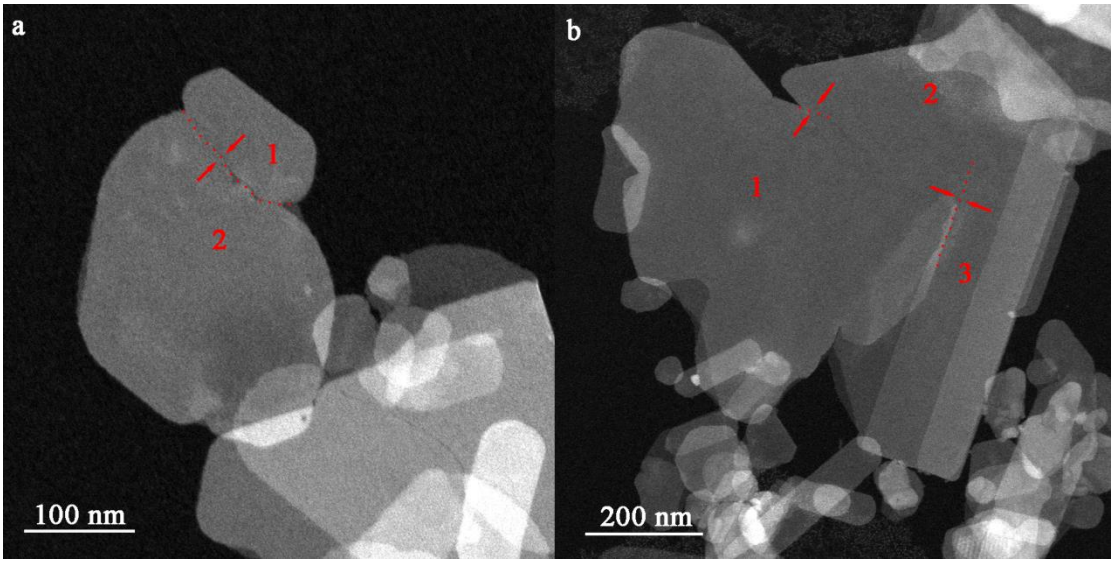

Fig. 10. STEM images of characteristic particle attachment in sample 220-500.

535 Table 1. Mean diameter in *ab*-plane of particles, α, β^2 of synthetic saponites. α and β^2
536 are the mean and variance of the natural logarithms of the observed diameters,
537 respectively.

Samples	Mean diameter (nm)	α	β^2
pMg220	87.2	4.24	0.454
pNi220	36.7	3.40	0.177
pMg220+pNi220	58.2	/	/
220-400	79.2	4.20	0.325
220-500	156.8	4.88	0.312

538
539
540